First-principles many-body study of the electronic and optical properties of CsK$_2$Sb, a semiconducting material for ultra-bright electron sources

Caterina Cocchi[1,2,4], **Sonal Mistry**[3], **Martin Schmeißer**[3], **Julius Kühn**[3] **and Thorsten Kamps**[1,3,4]

[1] Physics Department, Humboldt-Universität zu Berlin, Berlin, Germany
[2] IRIS Adlershof, Humboldt-Universität zu Berlin, Berlin, Germany
[3] Helmholtz-Zentrum Berlin, Berlin, Germany

E-mail: caterina.cocchi@physik.hu-berlin.de and kamps@helmholtz-berlin.de

CrossMark

Abstract

We present a comprehensive first-principles investigation of the electronic and optical properties of CsK$_2$Sb, a semiconducting material for ultra-bright electron sources for particle accelerators. Our study, based on density-functional theory and many-body perturbation theory, provides all the ingredients to model the emission of this material as a photocathode, including band gap, band dispersion, and optical absorption. An accurate description of these properties beyond the mean-field picture is relevant to take into account many-body effects. We discuss our results in the context of state-of-the-art electron sources for particle accelerators to set the stage towards improved modeling of quantum efficiency, intrinsic emittance, and other relevant quantities determining the macroscopic characteristics of photocathodes for ultra-bright beams.

Keywords: density-functional theory, electronic structure, theoretical spectroscopy, alkali antimonides

(Some figures may appear in colour only in the online journal)

1. Introduction

First-principles methodologies for electronic structure calculations have experienced impressive advances in the last few decades. While density-functional theory (DFT) [1, 2] remains the flagship method for *ab initio* modeling of ground-state properties, the state-of-the-art formalism for describing electronic and optical excitations is currently many-body perturbation theory (MBPT) based on Green's function approaches [3]. Band structures including the quasi-particle (QP) correction are obtained from the *GW* scheme [4–6] and absorption spectra, including excitonic effects, are computed from the solution of the Bethe–Salpeter equation (BSE) [7–9]. Owing to the quick progress and increasing power of available computational resources and infrastructures, MBPT, which is significantly more expensive than DFT [3], can now be routinely applied to realistic systems. This opportunity has produced a strong impact on many scientific and technological areas, including, as prominent examples, the development of materials for solar cells [10–12] and for energy storage [13, 14].

In light of these successful applications, it is natural to expect potential benefits from such advanced first-principles studies also for other tasks. For example, in the field of particle accelerator physics several groups around the globe are striving

[4] Authors to whom any correspondence should be addressed.

for photocathode growth optimization in view of enhancing the performance of semiconducting materials as electron sources for ultra-bright beams [15, 16]. Among them, it is worth mentioning the high brightness electron beam group at the Helmoltz-Zentrum Berlin working in the framework of the bERLinPro project [17, 18]. In this context, a hot topic concerns the optimal growth procedures of bi-alkali photocathodes, which have been reaching their maturity both as detectors and electron sources [19]. The main challenge lies in the reproducible growth of photocathodes with high quantum efficiency (QE), low transverse emittance, and long operational lifetime. Along with this issue, another open question to address urgently is the description of photoemission, which is the dominant emission mechanism considered for bright electron beam generation. In a typical photoelectron source, electrons are emitted by the photocathode, which is located inside an accelerating gap and illuminated by short laser pulses, so that the transverse and longitudinal shape and size can be controlled on a picosecond to femtosecond time scale via the drive laser pulse. The emitted electrons are rapidly accelerated to relativistic energies, thus partially mitigating the brightness deteriorating effects from space charge forces. The need to overcome the current technology largely based on metallic samples is dictated by the improved yield of emittance and QE of the photocathode necessary to achieve the high repetition rates that are required by free electron lasers, ultrafast diffraction and microscopy, inverse Compton scattering, and accelerator driven THz radiation sources [16, 20, 21]. To this end, insight from first-principles calculations is considered essential for the microscopic description of the electronic structure of these materials, which is the principal ingredient to model photoemission also on the macroscopic scale. However, it is reasonable to expect that the mean-field framework of DFT is not suitable for a quantitative representation of the complexity of the photoemission process in semiconductors. Above all, the determination of the band gap in these systems requires the inclusion of electron–electron correlation as provided by the *GW* approach. Likewise, electron–hole interactions may play a crucial role upon photon absorption, due to the relative low screening compared to metals. Also electron–phonon scattering mechanisms, representing the dominant processes in the diffusion of photo-excited electrons towards the surface, should be taken into account.

In this paper, we present a comprehensive study of the electronic and optical properties of CsK_2Sb, an exemplary crystalline material belonging to the family of multi-alkali antimonides, which are largely adopted as photocathodes [16, 22, 23]. Along with the detailed characterization of this system, the scope of this work is to demonstrate the capability of first-principles many-body methods to give insight into the electronic structure and excitations of this type of materials in view of their application as electron sources. For this purpose, we present an overview on the electronic properties of CsK_2Sb, including the analysis of the fundamental gap and of the character of valence and conduction bands, going beyond the mean-field picture provided by previous *ab initio* work on multi-alkali antimonides [24, 25]. We study the optical response in terms of the real and imaginary part of the dielectric function, discussing the role of the electron–hole interaction

in the photon absorption and analyzing the character of the excitations. Thanks to the capability of our approach to access core excitations on the same footing as the optical ones, we additionally investigate the x-ray absorption spectrum of CsK_2Sb from the Cs L_3-edge. This analysis offers additional information about the electronic structure of the system. We finally discuss the results of this *ab initio* many-body study in the context of the photocathode technology for particle accelerators with the goal of establishing a robust connection with the methods, the concepts, and the quantities that are typically investigated in theoretical condensed-matter physics.

2. Cesium potassium antimonide: a promising semiconducting material for bright electron sources

Photocathode materials commonly used for accelerator applications include metals and semiconductors, working within the ultra-violet (UV) and visible range of emitted light. Due to their high QE in the visible region, multi-alkali antimonides, such as CsK_2Sb (crystal structure shown in figure 1(a)), have been used since the 1960s as photon detectors, e.g. for Cherenkov light in cosmic rays as well as for particle detection [26]. The development of this class of photocathode materials was additionally driven by their robustness, low dark current, and short response time [16]. Photocathodes composed by Cs, K, and Sb atoms in varying stoichiometries (here indicated as Cs–K–Sb photocathodes) are particularly attractive for high current and low emittance photoinjection. Their small band gap (E_{gap}) and low electron affinity (EA), both of the order of 1 eV [27, 28], allow for photoemission close to threshold in the near-infrared (IR) or visible range, whilst at the same time sustaining a high QE. The sum of the band gap and of the EA corresponds to the *minimum energy for photoemission*, $E_{min} = E_{gap} + EA$, which in turn enters the expression of the normalized intrinsic emittance (ε_n) from the photocathode as follows:

$$\varepsilon_n = \sigma_x \sqrt{\frac{h\nu - E_{min}}{3mc^2}}. \quad (1)$$

In equation (1), σ_x is the root-mean-square beam width and $h\nu$ is the energy of the incident photon. In the denominator we find universal constants such as the electron mass and the speed of light. In the numerator, the difference between $h\nu$ and E_{min} corresponds to the *excess energy*. The intrinsic emittance from the emission process usually limits the brightness of the electron source. As ε_n depends on the excess energy, by minimizing this quantity also the emittance decreases accordingly. It was indeed demonstrated experimentally that Cs–K–Sb photocathodes exhibit such characteristics [29]. However, a reduced excess energy comes at the cost of a reduced QE. In fact, one can express the QE as a function of photon energy and minimum energy for photoemission:

$$QE \propto (h\nu - E_{min})^2. \quad (2)$$

Equations (1) and (2) together illustrate the trade-off between the QE and intrinsic emittance. We note, however, that in the
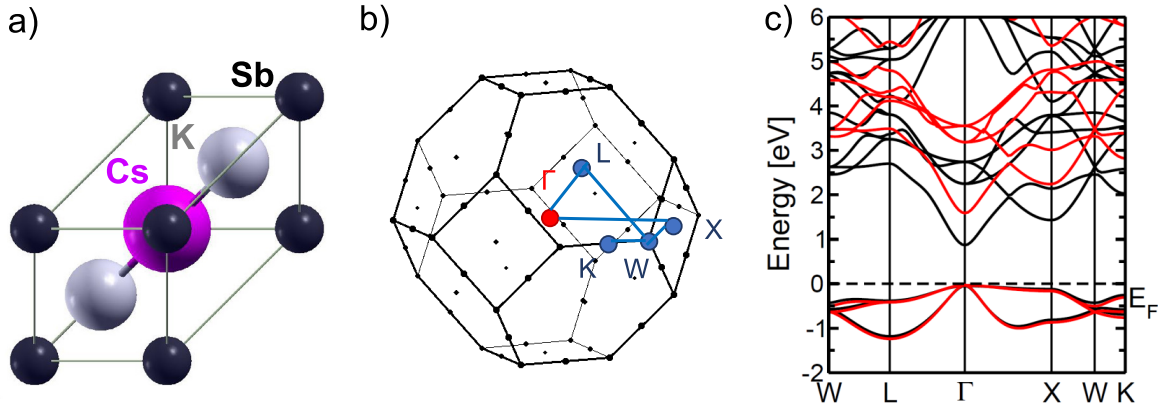
Figure 1. (a) Ball-and-stick model of the unit cell of CsK$_2$Sb with Cs atom in magenta, K atoms in grey, and Sb atoms in black. (b) Brillouin zone of CsK$_2$Sb with high-symmetry points and the path connecting them highlighted. (c) Band structure of CsK$_2$Sb computed from DFT (black lines) and within the single-shot G_0W_0 approximation (red lines). The Fermi energy (E_F) is set to zero at valence-band top.

presented form equations (1) and (2) were initially derived for metals based on a three-step model, accounting for (i) photon absorption, (ii) electron scattering, and (iii) photoemission [30, 31]. The main limitation of the three-step model is the absence of any specific information regarding the microscopic properties of the material. For instance, real photocathodes have a well defined crystal structure, often including polycrystalline domains, that needs to be considered. Likewise, changes in the electric potential from the bulk to the surface may critically affect the momentum of the emitted electrons. While the qualitative picture suggested by equations (1) and (2) can be extended to semiconductors, a quantitative description of intrinsic emittance and QE requires specific knowledge of the microscopic properties of the material, which differ substantially between metals and semiconductors. This is the type of information that the quantum-mechanical description of DFT and MBPT can provide, as demonstrated in the next sections. The ultimate goal is to develop an *ab initio*-based formalism in which microscopic features like structural properties, electronic structure, charge-carrier transport and scattering are consistently taken into account.

3. Theoretical background and computational details

Density-functional theory lays its foundation onto the Hohenberg–Kohn theorems [1] and is implemented according to the Kohn–Sham (KS) scheme [2], which consists of mapping the many-electron problem into a set of independent-particle equations for the electronic wave-functions of each electron i in the system:

$$\left[-\frac{\nabla^2}{2} + v_s(\mathbf{r}) \right] \varphi_i(\mathbf{r}) = \epsilon_i^{\mathrm{KS}} \varphi_i(\mathbf{r}), \qquad (3)$$

where ϵ_i^{KS} is the KS energy per particle. Equation (3) is expressed in atomic units, which are adopted from now on. On the left-hand side of equation (3), in addition to the

kinetic-energy operator, we find the effective potential per particle $v_s(\mathbf{r})$, which consists of the sum of three terms: $v_s(\mathbf{r}) = v_{\mathrm{ext}}(\mathbf{r}) + v_{\mathrm{H}}(\mathbf{r}) + v_{\mathrm{xc}}(\mathbf{r})$. The external potential v_{ext} includes the interaction between the negatively-charged electrons and the positively-charged nuclei. The Hartree potential $v_{\mathrm{H}}(\mathbf{r})$ accounts for the (mean-field) Coulomb between the electrons and $v_{\mathrm{xc}}(\mathbf{r})$ is the exchange-correlation (xc) potential. Since the exact form of $v_{\mathrm{xc}}(\mathbf{r})$ is unknown, this term in equation (3) has to be approximated. A reasonable approximation consists in treating exchange and correlation effects as in the homogeneous electron gas. This is given by the local-density approximation. In this work, we adopt the generalized gradient approximation (GGA) as implemented in the Perdew–Burke–Ernzerhof parameterization [32] and rely on MBPT for the description of excited-state properties, as detailed below. A relevant aspect in the solution of the KS equation (3) is the choice of the basis set. Here, we work in the framework of the linearized augmented planewave plus local-orbital (LAPW+lo) method, which allows for an explicit treatment of core electrons in addition to valence and conduction ones. An extensive description of this method is provided in [33].

Electronic properties and excitations are computed from MBPT with the DFT ground state as starting point. The *GW* approximation [4] is adopted in the single-shot perturbative approach G_0W_0 on top of the solutions of the KS equations [5]. In this way one can compute the electronic self-energy Σ that yields the quasi-particle (QP) energies of each electronic band $\epsilon_{i\mathbf{k}}$:

$$\epsilon_{i\mathbf{k}}^{\mathrm{QP}} = \epsilon_{i\mathbf{k}}^{\mathrm{KS}} + Z_{i\mathbf{k}} \left[\Re\Sigma_{i\mathbf{k}}(\epsilon_{i\mathbf{k}}^{\mathrm{KS}}) - V_{i\mathbf{k}}^{xc} \right], \qquad (4)$$

where $Z_{i\mathbf{k}}$ is the renormalization factor accounting for the energy-dependence of the self-energy. For the derivation of equation (4) and additional details we refer for review to [3, 34].

Optical and core excitations are computed from the solution of the BSE [35], which is the equation of motion for the two-particle electron–hole Green's function [7]. The matrix

form of the corresponding Schrödinger equation in the Tamm–Dancoff approximation reads:

$$\sum_{o'u'\mathbf{k}'} \hat{H}^{\text{BSE}}_{ou\mathbf{k},o'u'\mathbf{k}'} A^\lambda_{o'u'\mathbf{k}'} = E^\lambda A^\lambda_{ou\mathbf{k}},\tag{5}$$

where o and u labels initial occupied and final unoccupied states, respectively. In optical excitations initial states correspond to valence bands while upon x-ray absorption core electrons are excited to the conduction bands. In the latter case, the $\mathbf{k}$-dependence of the initial states drops (see for details [36]), although in equations (7) and (8) below it is retained for sake of generality. In spin-unpolarized systems, the effective two-particle Hamiltonian $\hat{H}^{\text{BSE}}$ is expressed by the sum of three terms:

$$\hat{H}^{\text{BSE}} = \hat{H}^{\text{diag}} + \hat{H}^{\text{dir}} + 2\hat{H}^x.\tag{6}$$

The *diagonal* term $\hat{H}^{\text{diag}}$ accounts for single quasi-particle transitions, neglecting the Coulomb interaction between electron and hole, which is instead included in the two remaining terms. The attraction between the positively-charged hole and the negatively-charge electron is given by $\hat{H}^{\text{dir}}$:

$$\hat{H}^{\text{dir}} = -\int d^3\mathbf{r}\int d^3\mathbf{r}'\phi_{o\mathbf{k}}(\mathbf{r})\phi^*_{u\mathbf{k}}(\mathbf{r}')W(\mathbf{r},\mathbf{r}')\phi^*_{o'\mathbf{k}'}(\mathbf{r})\phi_{u'\mathbf{k}'}(\mathbf{r}').\tag{7}$$

This integral contains the screened Coulomb interaction $W = \varepsilon^{-1}v$, where ε is the dielectric tensor of the system here computed within the random-phase approximation (RPA). The third term in equation (6), $\hat{H}^x$, represents the exchange interaction between the electron and the hole:

$$\hat{H}^x = \int d^3\mathbf{r} \int d^3\mathbf{r}'\phi_{o\mathbf{k}}(\mathbf{r})\phi^*_{u\mathbf{k}}(\mathbf{r})\bar{v}(\mathbf{r},\mathbf{r}')\phi^*_{o'\mathbf{k}'}(\mathbf{r}')\phi_{u'\mathbf{k}'}(\mathbf{r}'),\tag{8}$$

where $\bar{v}$ is the short-range part of the bare Coulomb potential accounting for local-field effects (LFE). These effects are particularly relevant in case of inhomogeneous materials, where the impinging electromagnetic field can trigger charge fluctuations on the interatomic scale and thus generate internal induced microscopic fields [3, 37, 38]. In the cubic CsK_2Sb crystal studied here, LFE are not expected to play a prominent role.

The BSE eigenvalues E^λ (equation (6)) yield *singlet* excitation energies. The exciton binding energy (E_b) of bound electron–hole pairs is often defined as the difference between excitation energies and the minimum direct band gap: $E_b = E^\lambda - E_{\text{gap}}$. This definition, however, does not apply to bound excitons above the absorption onset which can appear in complex materials, interfaces, and nanostructures (see, e.g. [39]). For this reason, we adopt an alternative and more general definition of E_b as the difference between the excitation energy computed by solving the BSE and obtained within the independent QP approximation (IQPA), i.e. retaining only $\hat{H}^{\text{diag}}$ in the Hamiltonian in equation (6). For bright excitons below the absorption onset the two definitions coincide.

The eigenvectors A^λ appear in the expression of the transition coefficients between each pair of occupied and unoccupied states:

$$\mathbf{t}^\lambda = \sum_{ou\mathbf{k}} A^\lambda_{ou\mathbf{k}} \frac{\langle o\mathbf{k}|\hat{\mathbf{p}}|u\mathbf{k}\rangle}{\varepsilon^{\text{QP}}_{u\mathbf{k}} - \varepsilon^{\text{QP}}_{o\mathbf{k}}}.\tag{9}$$

In the numerator of equation (9) we find the momentum matrix elements between initial and final states. In the denominator the difference between QP energies of each pair of initial and final states appear. For core excitations we take $\varepsilon^{\text{QP}}_{o\mathbf{k}} = \varepsilon^{\text{KS}}_o$. In this case, the $\mathbf{k}$-dependence vanishes and the QP correction is replaced by a scissors operator, due to the limitation of the G_0W_0 approximation to quantitatively reproduce core-level energies [36]. The transition coefficients from equation (9) enter the expression of the imaginary part of the macroscopic dielectric function representing the optical absorption of the material:

$$\Im\epsilon_M = \frac{8\pi^2}{\Omega}\sum_\lambda |\mathbf{t}^\lambda|^2\delta(\omega - E^\lambda).\tag{10}$$

In equation (10), Ω is the unit cell volume and ω the energy of the impinging photon. The real part of ϵ_M is related to the imaginary part by the Kramers–Kronig relations. The loss function is expressed by $\mathcal{L} = -\Im\epsilon_M^{-1}$.

The BSE eigenvectors A^λ of equation (5) contain information about the character and composition of the electron–hole pairs. They appear in the expression of the two-particle excitonic wave-function

$$\Psi^\lambda(\mathbf{r}_e, \mathbf{r}_h) = \sum_{ou\mathbf{k}} A^\lambda_{ou\mathbf{k}}\phi_{u\mathbf{k}}(\mathbf{r}_e)\phi^*_{o\mathbf{k}}(\mathbf{r}_h),\tag{11}$$

which is a six-dimensional quantity depending explicitly on the electron and the hole coordinates. In reciprocal space, we define the *weights* of the hole and the electron as:

$$w^\lambda_{o\mathbf{k}} = \sum_u |A^\lambda_{ou\mathbf{k}}|^2 \tag{12}$$

and

$$w^\lambda_{u\mathbf{k}} = \sum_o |A^\lambda_{ou\mathbf{k}}|^2,\tag{13}$$

respectively. Summations in equations (12) and (13) run over the range of occupied and unoccupied states included in the solution of equation (5). Details about the implementation of MBPT within the LAPW+lo formalism can be found in [36, 40–42].

All calculations presented in this work are performed with the `exciting` code [33]. The muffin-tin (MT) radii of all the atomic species involved (Cs, K, and Sb) are set to 1.65 bohr and a plane-wave basis-set cutoff $R_{\text{MT}}G_{\text{max}} = 8.0$ is employed. For ground-state calculations the Brillouin zone (BZ) is sampled using a homogeneous cubic $\mathbf{k}$-mesh with 8 points in each direction, corresponding to overall 29 points considering the symmetry operations. To calculate the quasi-particle band-structure within the G_0W_0 approximation, a $4 \times 4 \times 4$ $\mathbf{k}$-mesh is adopted without exploiting symmetries, for a total of 64 $\mathbf{k}$-points. The self-energy is computed by analytic continuation. In the BSE calculations for optical and x-ray absorption spectra, a Γ-shifted $\mathbf{k}$-mesh with 8 and 6 points in each direction is adopted, respectively. To compute

the screened Coulomb interaction within the RPA, 200 empty states are included. LFE are accounted for by employing about 59 $|\mathbf{G} + \mathbf{q}|$ vectors in the BSE calculations for optical spectra and about 300 in those for x-ray spectroscopy. Unit cells and BZs are visualized with the XCrysDen software [43].

4. Results

4.1. Electronic properties

We start our analysis by inspecting the electronic structure of CsK_2Sb, which is a face-centered cubic crystal including four atoms in its unit cell. The lattice parameter $a = 8.76$ Å has been obtained by performing volume optimization and fitting the results with the Birch–Murnaghan equation of state [44, 45]. This result is in agreement with the experimental value reported in [46] and with previous DFT predictions [24, 25], obtained, however, utilizing a different parameterization of the GGA xc functional. As shown in figure 1(a), the Sb atom is located at the origin $(0.0; 0.0; 0.0)$, while the Cs is in the center at $(0.5; 0.5; 0.5)$ and the two K are at $(\pm 0.25; \pm 0.25; \pm 0.25)$ [47]. The BZ is depicted in figure 1(b) with the Γ-point highlighted in red and the other high-symmetry points used in the band-structure plot in figure 1(c) marked in blue. There, the result obtained from G_0W_0 (red lines) is compared to the one from DFT (black lines). The two approaches yield very similar band structures: the valence bands coincide and the direct band gap is at Γ. Dispersion and effective masses in the conduction region are almost identical. The most striking difference, which is not surprising at all, is the size of the band gap. DFT gives a value of $0.92\,eV$ which is drastic underestimated compared to the G_0W_0 one of $1.62\,eV$, including the QP correction. Previously computed values of the band gap of CsK_2Sb exhibit a large variability, depending on the adopted approximations for the xc functional and the basis set. Results from the literature range from $0.58\,eV$ [47], to $0.80\,eV$ [25] up to $1.13\,eV$ [24]. In [25] additional estimates of $1.58\,eV$ and $1.99\,eV$ are obtained with the hybrid xc functionals proposed by Engel and Vosko [48] and Tran and Blaha [49], respectively. Both values are in line or slightly exceed the G_0W_0 result presented here. The few experimental references available for CsK_2Sb date back several decades ago. The early study by Nathan and Mee suggests for this material a band gap of $1.0\,eV$ and an electron affinity of $1.1\,eV$ [27]. Photoconductivity measurements by Ghosh and Varma, yielded a similar gap of $1.2\,eV$ [28]. Our G_0W_0 result of $1.62\,eV$, obtained for the ideal single crystal, infinitely periodic, and free from any defect or impurity at zero temperature, overestimates these values. However, it is hard to perform a comparison between theory and experiment in the absence of more recent and robust references. For this purpose, new measurements on high-quality samples grown under controlled conditions are required.

The character of the electronic bands is a crucial piece of information to identify the selection rules for allowed optical transitions, which are the first step of the photoemission process. For this purpose, we consider both the atom-projected density of states (DOS), shown in figure 2, and the QP band
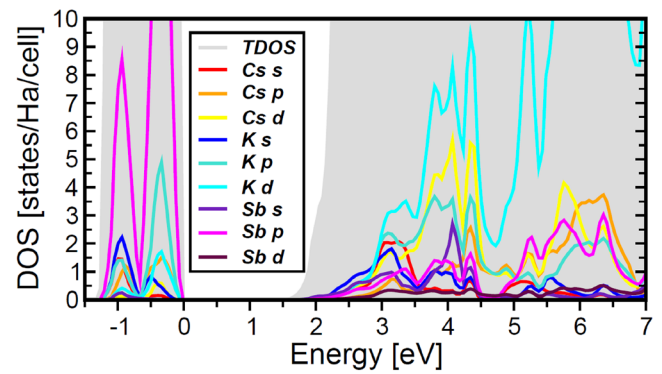

Figure 2. Total DOS (grey area) of CsK_2Sb, including the QP correction. Atom-projected electronic contributions are depicted in color. The Fermi energy is set to zero at valence-band top.

structures of CsK_2Sb with the atomic contributions (figure 3). One of the peculiarity of CsK_2Sb and, in general, of all alkali antimonides, is the limited number of valence states in the vicinity of the band gap (see figures 1(c) and 3). Lower-energy bands appear with almost flat dispersion at about $7.5\,eV$ below the Fermi energy (not shown), as discussed in previous works [24, 25, 47]. In line with the results of [24, 25, 47], obtained only at the DFT level, the three highest-occupied bands exhibit a clear *p*-character with contributions from the Sb atoms and, to less extent, from K and Cs *p*-states (figures 2 and 3). Potassium *s*-electrons also contribute, as shown in the DOS in figure 2. The conduction region, although strongly hybridized, is dominated by *d*-electrons, with the exception of the lowest-unoccupied band which has predominant *s*-character, as also suggested by its parabolic shape. The conduction-band minimum at Γ has hybridized Cs–Sb character, while along the X–W–K path most relevant contributions are given by Cs *s* electrons. Above $3.5\,eV$ in the energy scale of figure 3, Cs and K *d*-electrons dominate. Sb *d*-states hybridized with those bands also appear but their contribution is one order of magnitude smaller (the size of the circles in the corresponding plot in figure 3 is magnified by a factor of ten).

4.2. Optical properties

We now turn to the optical properties of CsK_2Sb. The dielectric function of this material was previously reported in [24, 25] for the ideal crystal and in [50] for the crystal under pressure. In these works, however, electron–hole correlation effects were not included. In figure 4(a) we show the absorption spectrum of CsK_2Sb computed from the solution of the BSE. Since equation (5) is solved by full diagonalization, we have access to the eigenvalues E^λ, representing the excitation energies marked by vertical lines in figure 4(a). In the same graph, we also show the IQPA spectrum which is analogous to the spectra reported in [24, 25]. The only difference is that here the initial and final states of the optical transitions include the QP correction computed from G_0W_0.

The absorption onset of CsK_2Sb lies in the visible region at $1.5\,eV$ and is given by a relatively weak peak, labeled A, formed by an exciton which is three-fold degenerate due to
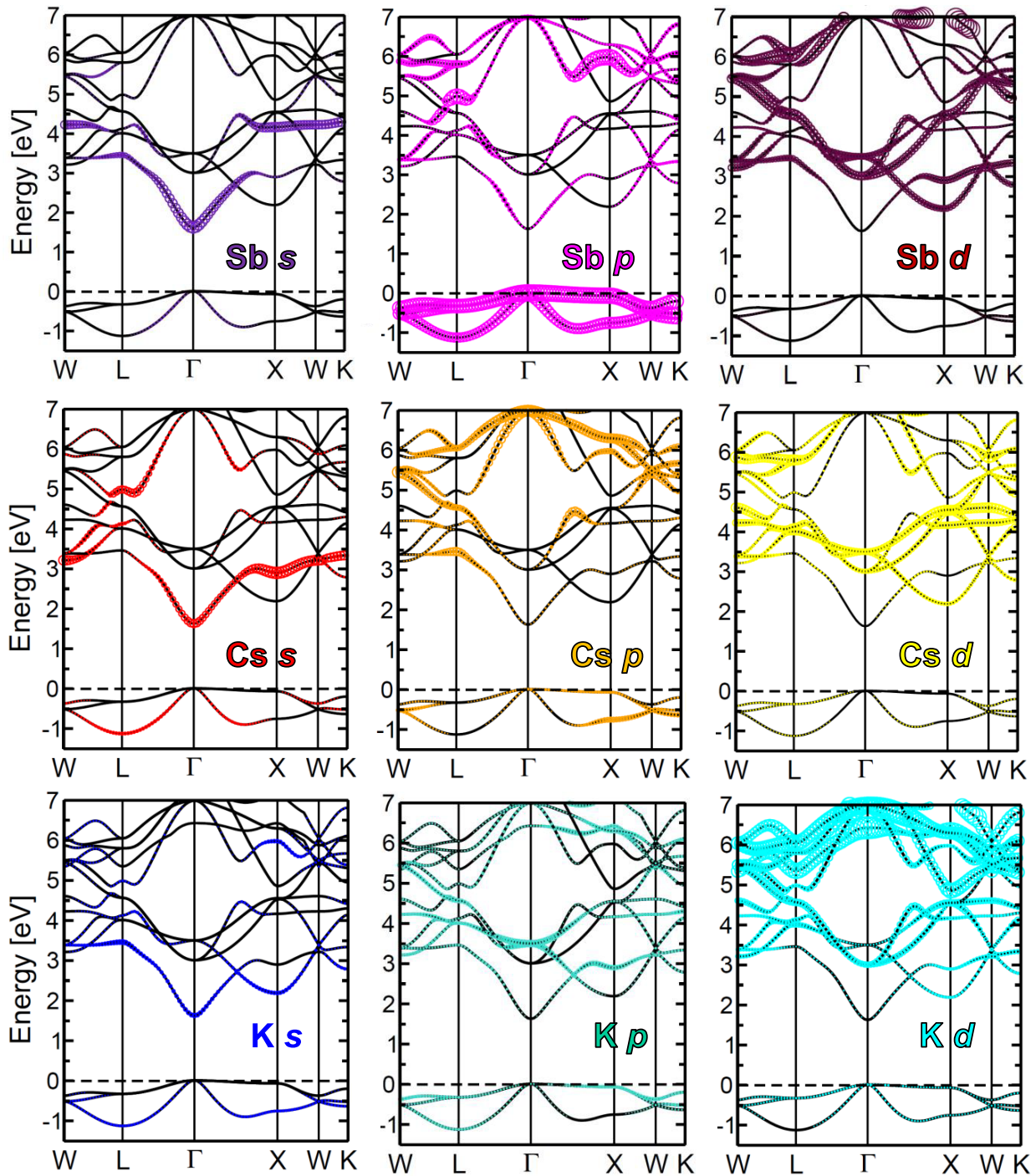
Figure 3. Band structure plots of CsK$_2$Sb, including the QP correction, showing the atom-projected character of the valence and conduction bands, quantified by the size of the colored circles. The contributions of Sb *d*-states are magnified by a factor of ten compared to all the others.

the cubic symmetry of the crystal. It stems from transitions between the valence-band maximum (VBM) and the conduction-band minimum (CBm) around the Γ-point (see figure 5) and has a binding energy of 120 meV. The second peak, labeled B, also lies in the visible region at approximately 2 eV. It is more intense than A and is formed by a manifold of excitations, which are again three-fold degenerate by crystal symmetry. The most intense excitations giving rise

to B emerge from interband transitions in the vicinity of the Γ-point, along the Γ-L and the Γ-X paths (figure 5). The electron–hole interaction acts on these excitation by enhancing their oscillator strength compared to the IQPA spectrum. Moreover, albeit peak B lies above the absorption onset, and, as such, the excitations forming it are conventionally not associated to bound excitons, their binding energy can be nonetheless estimated by comparing the position of this peak
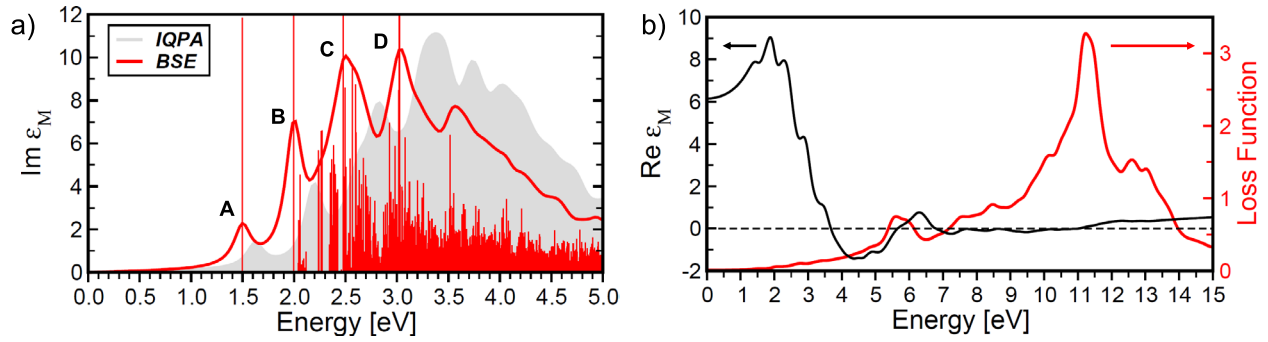
Figure 4. (a) Imaginary part of the macroscopic dielectric function of CsK$_2$Sb including excitonic effects (BSE, red line). Vertical bars indicate position and relative intensity of the solutions of the BSE. The spectra include a Lorentzian broadening of 100 meV mimicking the excitation lifetime. The first four peaks are labeled as A, B, C, and D respectively. For comparison, the spectrum without excitons, computed in the so-called independent quasi-particle approximation (IQPA, grey area), is also shown. (b) Real part of the macroscopic dielectric function (black) and loss function at $\mathbf{q} \to 0$ (red) computed from the BSE. A dashed line marks the zero in the scale of Re ε_M as a guide for the eyes. A Lorentzian broadening of 200 meV is applied.
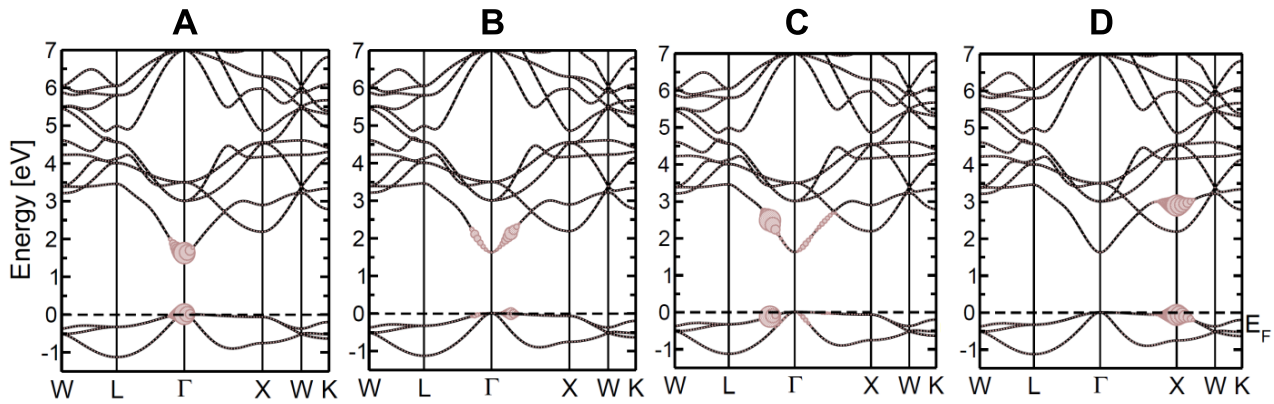

Figure 5. Band-structure contributions (circles, see equations (12) and (13)) of the excitons indicated in the optical absorption spectrum of figure 4(a). The QP correction is included and the Fermi energy (E_F) is set to zero at valence-band top.

with its IQPA counterpart as done in [39, 51]. The resulting binding energy is about 100 meV. The bound nature of these excitations is further indicated by their separation in energy from the continuum of excited states starting with peak C at approximately 2.5 eV. Also this peak is formed by a multitude of excitations. In figure 5 we report the band contributions to the most intense one, which corresponds again to a transition between the highest-occupied band and the lowest-unoccupied one but in this case along the Γ-L path. Also for the excitations forming the peak C the binding energies can be estimated in comparison with the IQPA spectrum and are of the order of a few hundred meV. The oscillator strength of peak C is enhanced when the electron–hole interaction is taken into account. A fourth peak, D, appears at the edge of the visible region at 3 eV. It is also red-shifted by a few hundred meV compared to its IQPA counterpart and, while formed by hundreds of BSE solutions, it is dominated by a few intense excitations. In figure 5, right panel, the composition of one of these excitations is shown: the dominant transitions are localized in the vicinity of the X point in the BZ. In the conduction region, target states belong to the second-lowest unoccupied band. By looking at figure 3, the Sb *p-d* character of these higher transitions is apparent. Conversely,

lower-energy peaks, formed by transitions in the vicinity of the Γ-point, have a prominent Sb *p-s* character. At higher energies, in the UV region, we find a continuum of excitations with almost homogeneously distributed spectral weight. Overall, the whole BSE spectrum plotted in figure 4(a) experiences a red-shift compared to the IQPA. As pointed out above, almost all peaks undergo a redistribution of their intensity, with the ones in the visible band gaining weight at the expenses of those in the UV band. These features indicate the relevant effects of the electron–hole interaction, which acts also above the absorption onset.

Excitations induced by higher-energy photons gives rise to collective electronic oscillations, which are commonly identified as plasmons. Plasmonic resonances appear in the loss function of CsK$_2$Sb at about 10 eV (figure 4(b)). Relevant features in this spectroscopic quantity are well above the visible region, at $\hbar\omega > 5$ eV. While local maxima appear between 5 and 9 eV, the most prominent peak in the loss function is at 11 eV. At this frequency, a pole in the real part of ϵ_M confirms the plasmonic nature of this excitation. In the low-energy region, instead, local oscillations in the real part of ϵ_M correspond to the absorption peak positions in the imaginary part (see figure 4(a)).
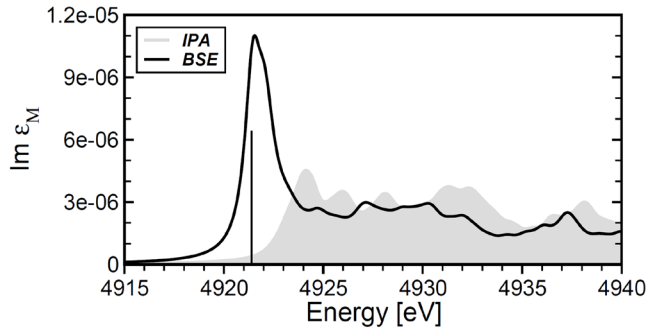
Figure 6. X-ray absorption spectrum of CsK_2Sb from the Cs L_3-edge given by the imaginary part of the macroscopic dielectric function computed from the solution of the BSE (black line). The vertical line marks the energy of the first excitons analyzed in figure 7. The result obtained in the independent-particle approximation (IPA) neglecting excitonic effects is also shown for comparison (grey area). A Lorentzian broadening of 500 meV is applied to both spectra.

4.3. Core excitations from the Cs L_3 edge

To complete the spectroscopic characterization of CsK_2Sb we turn to core excitations, focusing on transitions from the Cs L_3 edge. According to the selection rules for the quantum number *l*, target levels are Cs *s*- and *d*-states, which indeed dominate the bottom of the conduction region (see figures 2 and 3). The absorption spectrum is computed from the solution of the BSE with the set of initial states restricted to Cs $2p_{3/2}$ electrons. It is possible to decouple these transitions from those from the Cs $2p_{1/2}$ states due to their large spin–orbit splitting of a few hundreds eV. For comparison, we plot in figure 6 also the spectrum computed without the electron–hole interaction, in the independent-particle approximation (IPA). In this case, transitions are calculated directly from the KS states, not including the QP correction. The *GW* approximation is in fact unable to account for the QP correction of the extremely localized core states, which are typically underestimated by 10% of their energy in DFT. Adding the QP correction from G_0W_0 to the conduction bands, which is of the order of a few hundred meV, would thus not yield the correct absorption onset, which is indeed underestimated by roughly the same amount [36]. Also the spectrum shown in figure 6 suffers from this drawback. However, in the absence of experimental references, which typically guide the choice of an appropriate scissors operator (see, e.g. [52–54]), we decide to show the result of our calculation without the inclusion of any shift. From the difference between the KS core energy of Cs $2p_{3/2}$ electrons and reference values [55] and based on our experience [52–54], we expect the absorption onset in figure 6 to be underestimated by at least a few tens of eV compared to experiments. The analysis of the spectral features presented below is not affected by this choice.

The absorption onset of the BSE spectrum in figure 6 is characterized by a sharp maximum. In absolute units, its intensity is reduced by several orders of magnitude compared to the maxima in the optical absorption spectrum (figure 4). This difference is determined by the significantly smaller wavefunction overlap between conduction bands and core states
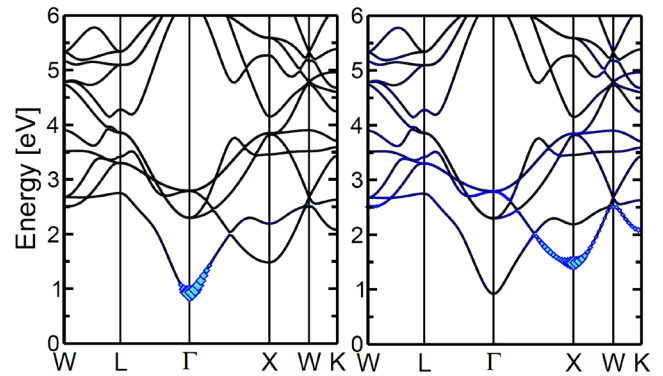

Figure 7. Conduction-band contribution (blue diamonds) of two (almost degenerate) excitons forming the sharp excitonic peak in the x-ray absorption spectrum of CsK_2Sb from the Cs L_3-edge, marked by the vertical bar in figure 6. The origin of the energy scale is set at the valence-band top.

compared to the valence ones. Concomitantly, the energy difference between the involved electronic levels is orders of magnitude larger. The numerator of equation (9) is therefore reduced while the denominator is increased. The comparison between the BSE spectrum and its IPA counterpart highlights the strong excitonic character of this peak. Overall, it is formed by 16 excitations with binding energies ranging between 150 and 200 meV. These values are about twice as large as those in the visible region, which is not surprising, given the more localized character of x-ray excitations compared to the optical ones. Here, excitonic effects manifest themselves mainly through the sizable redistribution of the spectral weight towards to the first peak. The IPA spectrum, obtained neglecting the electron–hole interaction, exhibits peaks of almost equal intensity, from the absorption edge up to 15 eV above it.

The band contributions to the first core bound excitons highlighted in the spectrum in figure 6 reveal that transitions to both *s*- and *d*-states are involved (see figure 7). The lowest-energy excitation corresponds to transitions to the CBm at Γ (figure 7(a)), which has a predominant *s*-character (see figure 3). Higher-energy excited states comprised in the first sharp peak are instead due to transitions to the band minimum at X, which has a distinct *d*-character. Non-negligible contributions also come from higher-energy bands (figure 7(b)). The coexistence of these excitations with different character within the first absorption peak makes the analysis of x-ray spectra from the Cs L_3 edge particularly promising for characterizing different phases and chemical compositions of cesium antimonides.

5. Discussion

The results presented above show the wealth of insight that first-principles many-body calculations can provide on the electronic structure of a material and its excitations. This information can be fruitfully exploited to model the characteristics of semiconducting photocathodes for particle accelerators. Band gap and electron affinity, the key parameters to estimate the intrinsic emittance of the cathode, can be reliably

computed only beyond the mean-field approach provided by semi-local DFT, which is unable to access excited-state properties. Adopting MBPT also allows to overcome the large variability of the DFT results related to different basis sets and xc functionals. Additional information about the electronic structure is given by the atomic character of the bands and their hybridization. These properties are crucial to understand the selection rules of optical and core-level spectroscopy. The optical absorption of CsK_2Sb, which spans the entire visible band, is characterized by excitonic effects also above the onset. Their role is to red-shift the maxima by a few hundred meV and to redistribute the oscillator strength towards the lower-energy peaks. The electronic transitions involved are mainly between the uppermost valence bands and the lowest conduction bands, with different contributions arising from various regions of the BZ, depending on the excitation energy. All these facets demonstrate that a simplistic description of the absorption process cannot capture the complex spectroscopic behavior exhibited by semiconductors. We have investigated x-ray absorption spectra of CsK_2Sb from the Cs L_3-edge, showing that also in this regime excitonic effects are dominant. In general, the ability of our first-principles many-body approach to selectively access core excitations from any atom and any edge is essential for achieving a comprehensive characterization of the material. Core spectroscopy represents in fact a powerful tool to probe the electronic structure of materials with atomic resolution, in order to detect the presence of defects, impurities, dislocations, and more.

In the context of electron sources for particle accelerators, the main quantities that determine the performance of a photocathode are the intrinsic emittance (equation (1)) and the QE (equation (2)), which estimates the amount of current that can be extracted from the material for given laser energy and power. Parameters like effective electron masses, absorption coefficients, and band gaps, which are typically extracted from *ab initio* calculations, can be substantially improved going beyond DFT and adopting the many-body framework presented here. For the case of CsK_2Sb analyzed here, the electronic band gap is at the lower edge of the visible region ($E_{gap} = 1.62$ eV) and the optical one a few meV below in the IR band. This energy window lies within the ideal absorption (and also emission) band for the optimal performance of a photocathode. Furthermore, the large effective masses of the lowest-unoccupied bands of CsK_2Sb ensure high mobility of the photo-excited charge carriers. The similar behaviors predicted already by DFT for related multi-alkali antimonides [24] hints that this entire class of materials is suitable for photocathode applications. The actual challenge, however, remains how to combine these quantities to realistically predict the performance of photocathodes remains a challenge. Photoemission is typically represented in a three-step picture initially designed for metallic cathodes [30], where the description of the whole process can be further simplified into a one-step model [56]. The extension of the three-step model to semiconducting electron sources requires appropriate extensions that take into account the specific mechanisms occurring in these materials. For instance, scattering events that are particularly relevant in photoemission, as (in

a semi-classical picture) they randomize the momentum distribution of the excited electrons, are mainly dominated by electron–phonon interactions in semiconductors. These processes cannot be modeled without having access to the microscopic properties of the material. Recent attempts to describe the transport of excited electrons towards the surface have been successfully carried out with Monte Carlo simulations for alkali antimonides [57, 58]. Dedicated *ab initio* studies focused on these types of interactions would further improve the current description and understanding of the photoemission process.

Extensive first-principles many-body studies of semiconducting materials for photocathodes like the one presented here are expected to bring significant benefits to the entire field of particle accelerator physics. The computational screening of a large number of compounds would further allow to identify systems with most promising characteristics in terms of QE. This information, combined with the knowledge of deposition parameters and other electron beam specifications, could contribute to tailor the properties of the cathode. For instance, one limiting factor in current photoinjector technology is the drive laser capability in the UV range. High-gain lasing is typically achieved in the IR region and then converted to UV by frequency up-conversion [59]. However, this process is not efficient. First-principles investigations could point to the necessary steps to tailor the electronic structure in order to shift the sensitivity to longer wavelengths, in view of ultimately designing and growing photocathodes operating in the IR range.

Further degrees of freedom in modeling materials for electron sources are surface effects, which have been the subject of an extensive computational work on metals [60]. Also semiconductors like alkali antimonides are characterized by highly reactive surfaces that are prone to contamination outside of ultra high vacuum conditions. Novel solutions are currently being explored to improve the lifetime of pure surface states. In a recent computational study based on DFT it was proposed to adopt protective monolayer coatings deposited on Cs_3Sb photocathodes, which are able to improved their lifetime by preventing surface contamination by residual gas [61].

6. Summary and conclusions

In summary, we have presented a comprehensive first-principles study of the electronic and optical excitations of CsK_2Sb, a semiconducting photocathode material for particle accelerators. We have characterized the band structure and the absorption spectrum in the framework of many-body perturbation theory, demonstrating the relevant role played by electron–electron and electron–hole correlation effects. With an estimated band-gap of about 1.6 eV, CsK_2Sb is confirmed to be a promising electron source. It absorbs visible light over the entire visible range where it exhibits excitonic effects that mainly consist in a slight redistribution of the oscillator strength towards low-energy maxima. We have analyzed the excitations in terms of band contributions, showing that transitions between the higher occupied and the lowest-unoccupied

bands dominate the absorption at visible wavelengths. This study in the optical region has been complemented by x-ray absorption spectroscopy computed from the Cs L_3-edge. The corresponding absorption edge is dominated by an intense excitonic peak stemming from transitions to unoccupied bands with both Cs *s*- and *d*-character.

The predictive power of the adopted methodology and the physical insight gained from the analysis of our results suggest a promising application of this approach to model photoemission from electron sources for particle accelerators. If the parameters obtained in this framework can be inserted directly in the existing models, the main challenge for future and more accurate studies consists in the extension of the model towards the inclusion of quantum-mechanical and many-body effects. This perspective can set the basis for an improved modeling of semiconducting photocathodes for particle accelerators and, concomitantly, extend the range of action of the methods of computational condensed-matter physics to systematically screen and investigate new materials for electron sources.

ORCID iDs

Caterina Cocchi ⓘ https://orcid.org/0000-0002-9243-9461
Martin Schmeißer ⓘ https://orcid.org/0000-0001-8426-3083
Julius Kühn ⓘ https://orcid.org/0000-0003-3744-9242
Thorsten Kamps ⓘ https://orcid.org/0000-0002-5122-2290

References

[1] Hohenberg P and Kohn W 1964 *Phys. Rev.* **136** B864
[2] Kohn W and Sham L J 1965 *Phys. Rev.* **140** A1133
[3] Onida G, Reining L and Rubio A 2002 *Rev. Mod. Phys.* **74** 601
[4] Hedin L 1965 *Phys. Rev.* **139** A796
[5] Hybertsen M S and Louie S G 1985 *Phys. Rev. Lett.* **55** 1418
[6] Hybertsen M S and Louie S G 1986 *Phys. Rev.* B **34** 5390
[7] Strinati G 1988 *Riv. Nuovo Cimento* **11** 1
[8] Hanke W and Sham L J 1980 *Phys. Rev.* B **21** 4656
[9] Rohlfing M and Louie S G 2000 *Phys. Rev.* B **62** 4927
[10] De Angelis F 2014 *Acc. Chem. Res.* **47** 3349
[11] Brenner T M, Egger D A, Kronik L, Hodes G and Cahen D 2016 *Nat. Rev. Mater.* **1** 15007
[12] Oba F and Kumagai Y 2018 *Appl. Phys. Express* **11** 060101
[13] Jain A, Shin Y and Persson K A 2016 *Nat. Rev. Mater.* **1** 15004
[14] Yoon G, Kim D-H, Park I, Chang D, Kim B, Lee B, Oh K and Kang K 2017 *Adv. Funct. Mater.* **27** 1702887
[15] Dowell D, Bazarov I, Dunham B, Harkay K, Hernandez-Garcia C, Legg R, Padmore H, Rao T, Smedley J and Wan W 2010 *Nucl. Instrum. Methods Phys. Res.* A **622** 685
[16] Musumeci P, Navarro J G, Rosenzweig J, Cultrera L, Bazarov I, Maxson J, Karkare S and Padmore H 2018 *Nucl. Instrum. Methods Phys. Res.* A **907** 209
[17] Abo-Bakr M *et al* 2017 *8th Int. Particle Accelerator Conf. (Copenhagen, Denmark, 14–9 May 2017) (*Geneva: JACOW) pp 855–8
[18] Neumann A *et al* 2018 *Proc. IPAC2018* (https://doi.org/10.18429/JACoW-IPAC2018-TUPML053)
[19] Dowell D *et al* 1993 *Appl. Phys. Lett.* **63** 2035
[20] Boucher S, Frigola P, Murokh A, Ruelas M, Jovanovic I, Rosenzweig J and Travish G 2009 *Nucl. Instrum. Methods Phys. Res.* A **608** S54
[21] Musumeci P, Moody J, Scoby C, Gutierrez M, Bender H and Wilcox N 2010 *Rev. Sci. Instrum.* **81** 013306
[22] Smedley J, Rao T and Wang E 2009 *AIP Conf. Proc.* **1149** 1062
[23] Schubert S *et al* 2013 *APL Mater.* **1** 032119
[24] Kalarasse L, Bennecer B and Kalarasse F 2010 *J. Phys. Chem. Solids* **71** 314
[25] Murtaza G, Ullah M, Ullah N, Rani M, Muzammil M, Khenata R, Ramay S M and Khan U 2016 *Bull. Mater. Sci.* **39** 1581
[26] Sommer A H 1956 *IRE Trans. Nucl. Sci.* **3** 8
[27] Nathan R and Mee C 1967 *Int. J. Electron.* **23** 349
[28] Ghosh C and Varma B 1978 *J. Appl. Phys.* **49** 4549
[29] Vecchione T, Ben-Zvi I, Dowell D, Feng J, Rao T, Smedley J, Wan W and Padmore H 2011 *Appl. Phys. Lett.* **99** 034103
[30] Berglund C N and Spicer W E 1964 *Phys. Rev.* **136** A1030
[31] Dowell D H and Schmerge J F 2009 *Phys. Rev. Spec. Top. Accel. Beams* **12** 074201
[32] Perdew J P, Burke K and Ernzerhof M 1996 *Phys. Rev. Lett.* **77** 3865
[33] Gulans A, Kontur S, Meisenbichler C, Nabok D, Pavone P, Rigamonti S, Sagmeister S, Werner U and Draxl C 2014 *J. Phys.: Condens. Matter* **26** 363202
[34] Aryasetiawan F and Gunnarsson O 1998 *Rep. Prog. Phys.* **61** 237
[35] Salpeter E E and Bethe H A 1951 *Phys. Rev.* **84** 1232
[36] Vorwerk C, Cocchi C and Draxl C 2017 *Phys. Rev.* B **95** 155121
[37] Wiser N 1963 *Phys. Rev.* **129** 62
[38] Aspnes D 1982 *Am. J. Phys.* **50** 704
[39] Aggoune W, Cocchi C, Nabok D, Rezouali K, Akli Belkhir M and Draxl C 2017 *J. Phys. Chem. Lett.* **8** 1464
[40] Puschnig P and Ambrosch-Draxl C 2002 *Phys. Rev.* B **66** 165105
[41] Sagmeister S and Ambrosch-Draxl C 2009 *Phys. Chem. Chem. Phys.* **11** 4451
[42] Nabok D, Gulans A and Draxl C 2016 *Phys. Rev.* B **94** 035118
[43] Kokalj A 1999 *J. Mol. Graph. Modelling* **17** 176
[44] Birch F 1947 *Phys. Rev.* **71** 809
[45] Murnaghan F 1944 *Proc. Natl Acad. Sci. USA* **30** 244
[46] Sommer A 1963 *Appl. Phys. Lett.* **3** 62
[47] Ettema A and de Groot R 2002 *Phys. Rev.* B **66** 115102
[48] Engel E and Vosko S H 1993 *Phys. Rev.* B **47** 13164
[49] Tran F and Blaha P 2009 *Phys. Rev. Lett.* **102** 226401
[50] Kalarasse L, Bennecer B, Kalarasse F and Djeroud S 2010 *J. Phys. Chem. Solids* **71** 1732
[51] Aggoune W, Cocchi C, Nabok D, Rezouali K, Belkhir M A and Draxl C 2018 *Phys. Rev.* B **97** 241114
[52] Cocchi C and Draxl C 2015 *Phys. Rev.* B **92** 205105
[53] Cocchi C, Zschiesche H, Nabok D, Mogilatenko A, Albrecht M, Galazka Z, Kirmse H, Draxl C and Koch C T 2016 *Phys. Rev.* B **94** 075147
[54] Vorwerk C, Hartmann C, Cocchi C, Sadoughi G, Habisreutinger S N, Félix R, Wilks R G, Snaith H J, Bär M and Draxl C 2018 *J. Phys. Chem. Lett.* **9** 1852
[55] Bearden J A and Burr A 1967 *Rev. Mod. Phys.* **39** 125
[56] Karkare S, Wan W, Feng J, Chiang T C and Padmore H A 2017 *Phys. Rev.* B **95** 075439
[57] Xie H, Ben-Zvi I, Rao T, Xin T and Wang E 2016 *Phys. Rev. Spec. Top. Accel. Beams* **19** 103401
[58] Gupta P, Cultrera L and Bazarov I 2017 *J. Appl. Phys.* **121** 215702
[59] Panuganti H and Piot P 2017 *Appl. Phys. Lett.* **110** 093505
[60] Camino B, Noakes T, Surman M, Seddon E and Harrison N 2016 *Comput. Mater. Sci.* **122** 331
[61] Wang G, Yang P, Moody N A and Batista E R 2018 *NPJ 2D Mater. Appl.* **2** 17